Toward Wave-based Sound Synthesis for Computer Animation

JUI-HSIEN WANG, Stanford University
ANTE QU, Stanford University
TIMOTHY R. LANGLOIS, Adobe Research
DOUG L. JAMES, Stanford University

We explore an integrated approach to sound generation that supports a wide variety of physics-based simulation models and computer-animated phenomena. Targeting high-quality offline sound synthesis, we seek to resolve animation-driven sound radiation with near-field scattering and diffraction effects. The core of our approach is a sharp-interface finite-difference time-domain (FDTD) wavesolver, with a series of supporting algorithms to handle rapidly deforming and vibrating embedded interfaces arising in physics-based animation sound. Once the solver rasterizes these interfaces, it must evaluate acceleration boundary conditions (BCs) that involve model- and phenomena-specific computations. We introduce *acoustic shaders* as a mechanism to abstract away these complexities, and describe a variety of implementations for computer animation: near-rigid objects with ringing and acceleration noise, deformable (finite element) models such as thin shells, bubble-based water, and virtual characters. Since time-domain wave synthesis is expensive, we only simulate pressure waves in a small region about each sound source, then estimate a far-field pressure signal. To further improve scalability beyond multi-threading, we propose a fully *time-parallel sound synthesis* method that is demonstrated on commodity cloud computing resources. In addition to presenting results for multiple animation phenomena (water, rigid, shells, kinematic deformers, etc.) we also propose 3D automatic dialogue replacement (3DADR) for virtual characters so that pre-recorded dialogue can include character movement, and near-field shadowing and scattering sound effects.

CCS Concepts: • **Computing methodologies** → *Physical simulation*;

Additional Key Words and Phrases: Computer animation, sound synthesis, finite-difference time-domain method, acoustics

1 INTRODUCTION

Recent advances in physics-based sound synthesis have led to improved sound-generation techniques for computer-animated phenomena, including water, rigid bodies, deformable models like rods

Authors' addresses: Jui-Hsien Wang, Stanford University, jui-hsien.wang@stanford.edu; Ante Qu, Stanford University, antequ@cs.stanford.edu; Timothy R. Langlois, Adobe Research, tlangloi@adobe.com; Doug L. James, Stanford University.

and shells, fire, and brittle fracture. However, unlike visual rendering techniques which are slow but capable of generating very high-quality, general-purpose results during parallel offline rendering, current methods for sound synthesis suffer from several fundamental deficiencies that limit high-quality renderings. First, because of the high space-time complexity of sound modeling and complicated acoustic phenomena, many modeling approximations (linearizations, simplified radiation, etc.) and algorithmic optimizations (precomputation, data-driven methods, etc.) are typically made for tractability and to improve performance, but can limit sound quality and the range of physical phenomena that can be considered. Second, the proliferation of real-time, object-level and/or phenomena-specific sound models has led to a lack of integrated wave modeling, wherein it is difficult to combine models and have them support inter-model acoustic interactions, such as shadowing and scattering. The end result is that there is no practical general-purpose solution (regardless of performance) for practitioners to author general animations with integrated sound synthesis. In contrast, we seek a general rendering approach where, given an animation, say of a crash cymbal being hit (see Figure 1), one can just "hit the render button and wait," to get the high-quality result.
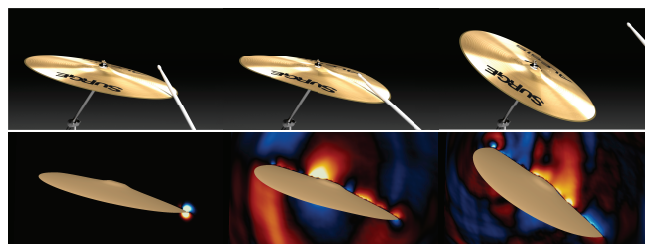

Fig. 1. **Crash! Sound waves radiate off a visibly deforming crash cymbal:** Our sharp-interface finite-difference time-domain (FDTD) wave solver can synthesize sound sources with rapidly deforming interfaces, such as this thin-shell model, or even water, using a single integrated approach.

In this paper, we explore offline wave-based sound synthesis techniques that can generate high-quality animation-sound content for general-purpose dynamic scenes and multi-physics sound sources. The general-purpose integrated approach is inherently extremely slow, but enables "what if" exploration of the rich range of sounds possible from complex animated phenomena (such as splashing water), and to better understand future challenges and needs for animation sound. We humbly liken our approach to early "what if" digital image synthesis efforts three decades ago, such as the "one frame movie" generated in the '80s by the aspiring REYES ("Renders Everything You Ever Saw") 3D rendering system [Cook et al. 1987] that "demonstrated, at least theoretically, the possibility of creating
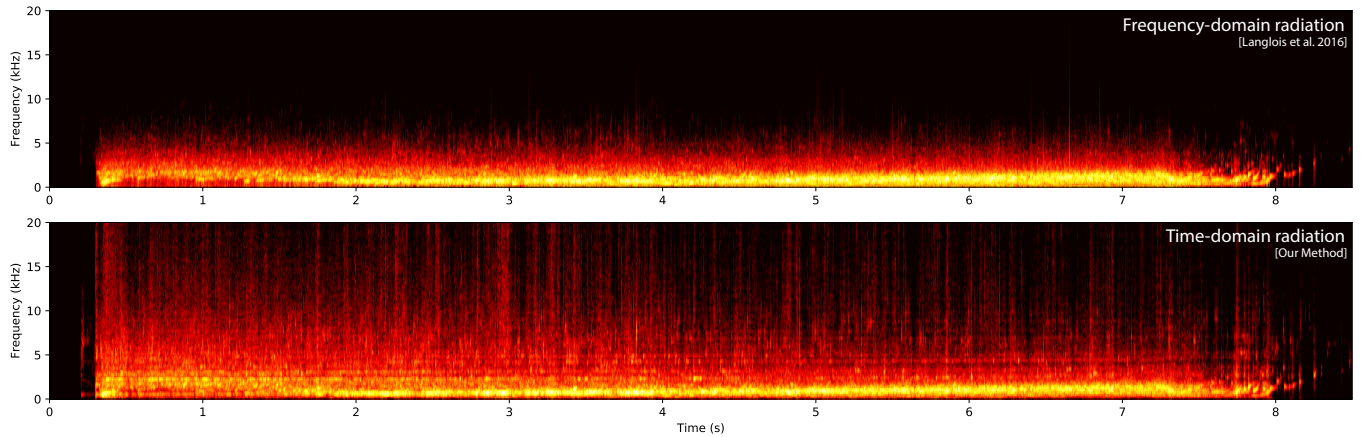
Fig. 2. **Dramatically Improved Water Sounds:** (Bottom, left) Using water simulation and surface vibration data from [Langlois et al. 2016], we simulated (Bottom, right) acoustic waves emitted from the rapidly deforming and vibrating fluid-air interface using our FDTD solver *(in this 2D slice, the rigid container is colored black, and the water is solid blue)*. Interactions with the container and water surface geometry cause complex time-varying radiation patterns, cavity resonances, and dramatically enhance the sound compared to the prior frequency-domain bubble radiation model. Spectrograms clearly demonstrate (Top) missing high-frequency detail in the prior approach whereas (Middle) our approach produces renderings with enhanced high-frequency content, that tend to produce more natural water sounds that are less harsh.
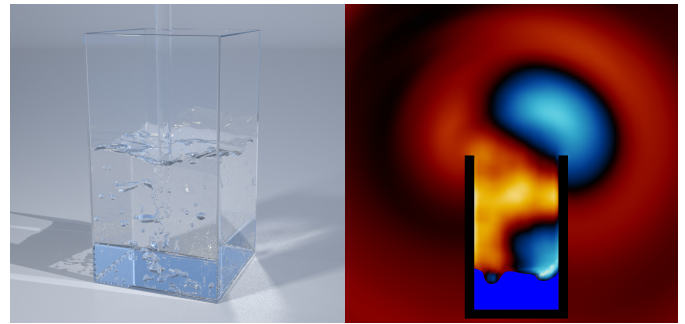
full length sequences, or even a feature film, composed of images which matched the quality of 35mm film" [Cook 2015], as opposed to a tweak on existing rendering methods [Heckbert 1987]. The theme of this paper is to first know what we want to compute and how, and then, later, we will optimize, design, and build parallel systems to do it fast. Our initial explorations have already shown a vastly richer class of sounds are possible, such as for bubble-based water animations (see Figure 2).

To resolve complex sound radiation, near-field scattering and diffraction effects, we rely on a general-purpose pressure-based finite-difference time-domain (FDTD) wavesolver. We describe a series of methods to support embedded geometric interfaces and to impose Neumann (acceleration) boundary conditions (BCs) on them using a ghost-cell technique. Once the solver rasterizes these interfaces, it then evaluates the acceleration BCs prescribed by model- and phenomena-specific computations (assuming a one-way coupling "animation to sound" approach). We introduce *acoustic shaders* as a computational abstraction of the various simulation-level details needed to evaluate (usually Neumann acceleration) BCs at audio-sample rates. An overview of our approach is shown in Figure 3. We describe a variety of shader implementations for physics-based computer animation: near-rigid (modal) objects, deformable (finite element) objects such as thin shells, acceleration noise, bubble-based water, and various sound sources, e.g., for virtual characters.

Since FDTD wave synthesis is expensive for source modeling due to the fine spatial grids needed to resolve geometry, and the small CFL-based timestep restriction, we only simulate pressure waves in
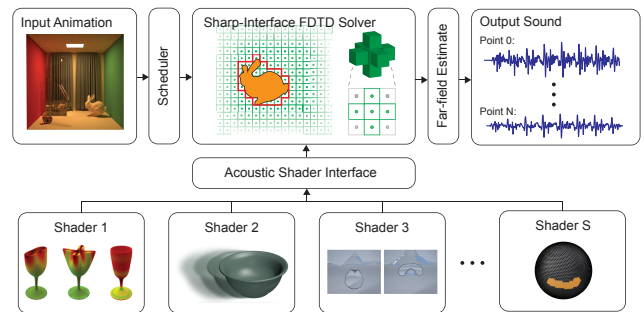
Fig. 3. **System Overview:** Our wave-based sound synthesis framework uses a pressure-based FDTD solver (§3) to resolve near-field acoustic waves radiating from animation-sound sources. A practical far-field pressure estimator generates sound signals at the listening point (§5). We use "acoustic shaders" (§4) to evaluate boundary condition (BC) data, thereby encapsulating simulation-level sound-source details, and enabling efficient BC sampling by the FDTD solver on rasterized embedded interfaces. A parallel-in-time algorithm is used to schedule solves for scalable simulation (§6).

a small box-like region of interest around the sound source, with an enclosing acoustically absorbing layer to remove out-going waves. For each domain, a far-field pressure expansion is estimated from multiple pressure samples along any out-going listener ray, for use by a listener or external auralization engine. Our wave-solver can synthesize many complex sounds, but it is still slow. To improve

performance beyond thread-level parallelism, we demonstrate a *time-parallel* method for sound-source evaluation that exploits the linear dependence of the sound on the nonzero boundary data. Finally, we demonstrate various results for rigid bodies, nonlinear thin shells, water, etc., evaluated using commodity cloud computing resources. In addition, we demonstrate 3D automatic dialogue replacement (3DADR) for virtual characters that processes pre-recorded dialogue to include character movement, and near-field shadowing and scattering sound effects.

2 RELATED WORK

Sound rendering has a long history in computer graphics and animation [Takala and Hahn 1992] and interactive virtual environments [Begault 1994]. While most sound effects can be achieved using recordings, data-driven methods, procedural audio effects, and other creative means, there is a long history in computer sound and music of physics-based methods used for non-visual/audio-only sound generation [Cook 2002; Gaver 1993; Smith 1992]. The process by which a sound field in a virtual space is rendered audible to a binaural listener at a specific position in space is referred to as *auralization* [Kleiner et al. 1993; Vorländer 2008], and for practical reasons it is usually broken into three stages: (1) sound generation/synthesis, (2) sound propagation throughout the scene, and (3) binaural listening. Our approach concerns the first stage (sound generation for offline computer animation), but also touches on near-field sound propagation and related numerical wave simulation techniques. In offline computer animation, most sound tracks are composed using digital audio workstations (DAWs), such as Pro Tools [Avid Technology 2018], which can record and mix audio, and apply various effects (such as reverb) during audio post production. Our approach is complementary to existing methods, in that it enables another way to generate (3D) sound clips that are synchronized with animated content.

Prior works on animation-sound have modeled sound radiation from animated solids and fluids in a wide variety of ways, ranging from completely ignoring it, to approximating in any number of ways for convenience and speed. Rigid-body sound models based on decoupled linear modal oscillators have been widely considered since the '90s [Cook 2002; van den Doel and Pai 1998], and have long enjoyed real-time performance and acceleration [Bonneel et al. 2008]. Detailed wave radiation is usually ignored, with the amplitude of the oscillators displayed directly, possible with calibration from recordings [van den Doel et al. 2001] or material parameters hand tuned for plausibility [O'Brien et al. 2002].

Precomputed acoustic transfer [James et al. 2006] was introduced to provide real-time estimation of acoustic pressure amplitudes for harmonic modal vibrations, and leveraged precomputed radiation solutions to the Helmholtz equation. While the method could account for realistic sound amplitudes from linear modal vibration models, it had several shortcomings including assumptions of linearized small-amplitude modal dynamics, pure harmonic oscillations (which poorly approximate the transients following contact events), and the inability of nearby objects to influence each other acoustically, e.g., shadowing and interreflections. All of these assumptions are no longer necessary using our general FDTD synthesis framework.

Precomputed acceleration noise [Chadwick et al. 2012a,b] was introduced to account for transient "clicking" sounds due to hard rigid-body accelerations that dominate ringing (modal) noise for small objects. The approach also used a FDTD method to estimate far-field radiation. However, we do not precompute these object-specific separate responses for interactive performance, but instead compute both ringing (modal) and acceleration noise effects on-the-fly simultaneously using a single wavefield in our general FDTD synthesis framework.

O'Brien et al. [2001] also proposed a time-domain sound synthesis framework that could render audio-rate vibrations of nonlinear deformable finite-element models, employing a ray-based attenuated delay-line model of radiation. While slow at the time (primarily due to high explicit time-stepping costs of nonlinear FEM models) a very wide variety of animations and sounds were possible. We propose a wave-based FDTD framework that more accurately accounts for soundwave radiation (and scattering). Although the computational cost is higher, wave phenomena are critical to predictive modeling of realistic radiated sounds.

More complex animation-sound phenomena have been considered that would also benefit from our high-quality FDTD sound synthesis framework. Efficient reduced-order models of near-rigid thin shells were considered in [Chadwick et al. 2009], but could not simulate large deformations (due to mode locking). Furthermore, the linear acoustic transfer model is technically incorrect since the modal oscillators are not frequency localized due to nonlinear mode coupling. Schweickart et al. [2017] synthesized sounds from elastic rods, and supported large deformations, such as for a Slinky falling down stairs, and used a precomputed dipole radiation model, but did not support scattering nearby surfaces or itself. Cloth and paper sound synthesis have been explored using various highly specialized techniques which address challenges due to the difficulty of direct numerical simulation of highly nonlinear deformations, vibrations, and acoustic emissions [An et al. 2012; Cirio et al. 2016; Schreck et al. 2016]. Chadwick and James [2011] synthesized combustion sounds using a hybrid simulation and data-driven approach. In contrast, our approach supports radiation from highly deforming interfaces, makes no assumptions about the underlying vibration model or linearity, and can capture full spectrum behavior, possibly removing the dependence on data-driven techniques.

Zheng and James [2010] synthesized brittle fracture sounds using rigid-body sound models based on linear modal analysis and precomputed acoustic transfer. Unfortunately every fracture event invalided the precomputed models, and led to expensive acoustic transfer re-computations. In contrast, by resolving each object's sound radiation on a shared FDTD wavefield grid, extensive precomputation of object-specific sound radiation models can be avoided.

The modeling of water sounds goes back to Minnaert's classical bubble vibration model [Minnaert 1933], which van den Doel [2005] used in modal sound banks for real-time audio-domain synthesis of stochastic water sounds without radiation modeling. Similar single-frequency bubble models were considered [Moss et al. 2010; Zheng and James 2009]. The latter method explored a per-bubble Helmholtz acoustic transfer model to better estimate the sound radiation, resulting in thousands of exterior fast multipole Helmholtz radiation solves per animation-sound clip. Improved two-phase

incompressible fluid-air modeling, and capacitance-based bubble frequency estimation were introduced in [Langlois et al. 2016], and combined with an acoustic transfer model similar to [Zheng and James 2009]. In contrast, we use a FDTD solver to better account for the air-borne sound waves, and the related transient radiation and scattering details which are perceptually significant (see Figure 2). While FDTD solves are expensive, they can actually be far cheaper (but less parallel) than the thousands to millions of per-bubble exterior Helmholtz radiation solves, since the radiation of all bubbles are resolved simultaneously by one FDTD wave simulation.

Methods for sound propagation modeling in interactive virtual environments have been explored for decades, and are increasingly used to produce interactive reverb effects for point-like sound sources, e.g., of a sound recording. For large architectural and outdoor environments, geometric propagation techniques (e.g., ray-based methods) are most popular for approximating occlusion and scattering effects. Examples include methods based on beam tracing [Funkhouser et al. 1998, 1999], or frustum tracing [Chandak et al. 2008], extensions to capture diffraction around corners using the uniform theory of diffraction [Tsingos et al. 2001], higher-order diffraction effects [Schissler et al. 2014], or hybrid approach based on spatial/frequency decomposition [Yeh et al. 2013]. Wave-based sound propagation techniques are less practical for interactive applications unless precomputations and approximations are used: notable recent innovations include adaptive rectangular decompositions [Raghuvanshi et al. 2009], equivalent source approximations [Mehra et al. 2013], and parametric wave field coding [Raghuvanshi and Snyder 2014]. For performance reasons, and to admit preprocessing, methods often make assumptions, such as a static environment. In contrast, our work applies to offline sound source modeling in smaller domains where strong diffraction and wave effects preclude the use of geometric/ray-based approaches, and highly deforming interfaces and animated phenomena preclude the use of many precomputation techniques.

Finite-difference time-domain (FDTD) methods [Larsson and Thomée 2009] and digital waveguides [Smith 1992] have long been used to approximate solutions to the wave equation, and fundamental stability and accuracy bounds are relatively well understood. Thanks to computational advances, a number of recent papers have started to use FDTD methods to solve wide-bandwidth acoustic radiation problems in applications such as computational room acoustics [Bilbao 2013], musical instrument design [Bilbao 2009], and head-related transfer function computation [Meshram et al. 2014]. Due to advanced parallel hardware such as GPUs and the scalable performance of FDTD, there are also a number of recent papers exploring the use of FDTD methods to achieve high-throughput [Mehra et al. 2012; Micikevicius 2009] or even real-time wave simulation [Allen and Raghuvanshi 2015], as well as using large GPU clusters to perform fast seismic modeling (elastic waves) [Komatitsch et al. 2010] and electrodynamics simulations [Taflove and Hagness 2005]. Particularly noteworthy is the work at the University of Edinburgh by Stefan Bilbao, Craig Webb and others on GPU-accelerated FDTD sound simulations of musical instruments, such as a timpani drum [Bilbao and Webb 2013], a snare drum [Bilbao 2011], and digital musical arrangements (see Webb's Ph.D. thesis [Webb 2014]), which is similar

in spirit to our general-purpose approach, although we can not rely on rigid, rasterized geometry in computer animation.

Simulating acoustic waves in a dynamic environment is less explored. A notable exception is the paper by Allen et al. [2015], which simulates virtual instruments that can have time-varying geometric features, such as opening and closing of tone holes. The geometry transition was made smooth by the use of a time-varying perfectly matched layer (PML), which blends the momentum equation and boundary condition enforcement. Although it works well for creating/removing walls for the instrument, the blending function can affect the transients of the sound and this formulation seems ill-suited for handling general rigid-body transformations and object deformations for animation.

3 ACOUSTIC WAVE SOLVER

We now describe the core FDTD acoustic wave solver used in our approach, beginning with some background material (§3.1). To compute high-quality, low-noise pressure signals, we employ a high-order boundary sampling method for enforcing the Neumann boundary conditions. The method is explained in §3.2 and §3.3, where we discuss the accurate acoustic BC enforcement on static interfaces using a ghost-cell formulation, and the time-consistent interface tracking method, respectively.

3.1 Background Material on FDTD Acoustics

Acoustic Wave Equation. Consider a simple scene with a single (dynamic) object, O. Let $\Omega \subset \mathbb{R}^3$ be the open set containing the surrounding acoustic medium, and Γ be the boundary of this set restricted to O's surface. Pressure perturbations in Ω are governed by the acoustic wave equation

$$\frac{\partial^2 p(\boldsymbol{x}, t)}{\partial t^2} = c^2 \nabla^2 p(\boldsymbol{x}, t) + c\alpha \nabla^2 \frac{\partial p(\boldsymbol{x}, t)}{\partial t}, \quad \boldsymbol{x} \in \Omega, \qquad (1)$$

where c is the speed of sound in the medium (343.2 m/s in air at standard temperature and pressure), and α is a constant coefficient that controls damping from air viscosity (derived from linearizing the Navier-Stokes equation [Morse and Ingard 1968; Webb and Bilbao 2011]). The Neumann boundary condition enables surface accelerations to generate waves:

$$\partial_n p(\boldsymbol{x}, t)(\boldsymbol{x}) = -\rho a_n(\boldsymbol{x}, t), \quad \boldsymbol{x} \in \Gamma, \qquad (2)$$

where ρ is the medium density (1.2041 kg/m^3 for air), $\boldsymbol{n}$ is the normal vector at the surface position, $\partial_n p(\boldsymbol{x}, t)$ is the normal pressure gradient and a_n is the normal surface acceleration. Intuitively, nonzero surface acceleration on O leads to pressure disturbances, which travel outwards through Ω and are perceived as sound when they reach our ears. The linear wave equation is valid whenever O's boundary velocity is much lower than c, which is true in our application domain.

Finite-difference simulation. We solve the wave equation using the finite-difference time-domain method (FDTD) [Larsson and Thomée 2009] on a regular, collocated pressure grid. We use the standard 2nd-order centered difference in space and time. Specifically, suppose we allocate a grid of cell size h and time step size τ, then the pressure

update at cell (i, j, k) can be expressed as

$$p_{i,j,k}^{n+1} = (2 + (c^2\tau^2 + c\alpha\tau)\tilde{\nabla}^2)p_{i,j,k}^n - (1 + c\alpha\tau\tilde{\nabla}^2)p_{i,j,k}^{n-1}, \quad (3)$$

where $p_{i,j,k}^n \equiv p(ih, jh, kh, n\tau)$ is the discretized pressure. $\tilde{\nabla}^2$ is the 7-point discrete Laplacian defined as

$$h^2\tilde{\nabla}^2 p_{i,j,k} = p_{i-1,j,k} + p_{i+1,j,k} + p_{i,j-1,k} + p_{i,j+1,k} \quad (4)$$
$$+ p_{i,j,k-1} + p_{i,j,k+1} - 6p_{i,j,k}. \quad (5)$$

The grid cell size, h, is selected based on the scene and the desired frequency resolution (see §7.1.1). Given h, the time step size, τ, is chosen as the maximum value that satisfies the stability bound, $\tau c \leq \sqrt{\alpha^2 + h^2/3} - \alpha$, set by the Courant-Friedrichs-Lewy (CFL) condition in 3D [Bilbao 2009]. Note that to leading order, the time step size is proportional to the cell size.

Absorbing Boundary Conditions. When performing FDTD acoustic wave simulations in a finite domain, it is typical to implement either absorbing boundary conditions (ABCs) [Clayton and Engquist 1977] or perfectly matched layers (PMLs) [Chadwick et al. 2012b; Liu and Tao 1997] at the grid boundary to minimize artificial reflections. To accommodate moving objects and to maintain consistency with the pressure collocated grid, we adopt the computationally simpler Engquist-Majda type ABC [Bilbao 2011; Engquist and Majda 1977]. More specifically, we have found that a split-field PML [Liu and Tao 1997], which relies on staggered pressure-velocity grids, can cause interpolation inconsistency if an object passes through the grid boundary (see §3.3). In contrast, the EM-ABC allows us to more aggressively place small domains around localized sound sources. For example, for 3D dialogue re-recording, we can place a domain just around a character's head, with the torso passing through the domain boundary without causing problems. Please see Appendix B for more details on the ABC implementation.

3.2 Accurate Object Interface Tracking

We describe a high-order boundary sampling method for enforcing the Neumann BC (2) in this section. Compared to a 1st-order staircasing boundary approximation, our method tracks the positions of the embedded interfaces on the subgrid level and respects the surface normals when discretizing BCs, which results in smoother scattering field, less distorted radiation patterns (Figure 4), and resolves more high-frequency content (Appendix C). Compared to other high-order boundary handling methods in acoustics literature, our method has smaller overhead as there is no need to remesh the domain [Bilbao 2013; Botteldooren 1994] or determine cut-cell volumes [Tolan and Schneider 2003]. Other local conforming methods [Häggblad and Engquist 2012] might not generalize well to non-zero BCs and dynamic scenes. Our method has the spirit of the immersed boundary methods in computational fluid dynamics [Fedkiw et al. 1999; Mittal et al. 2008; Mittal and Iaccarino 2005; Peskin 1981], where the effects of the boundaries are computed and stored directly on the grid. Because no remeshing is required, it is ideal for dynamic simulations. We modified the method from [Mittal et al. 2008] for acoustic simulation on a pressure collocated grid. In addition, we avoided the ill-conditioned local solves by hybridizing 1st- and 2nd-order boundary handling to maximize solve efficiency.
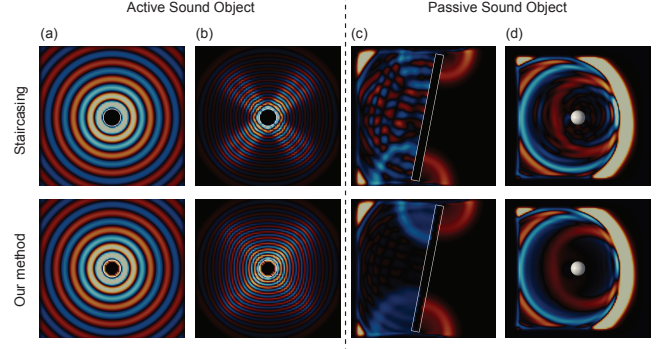

Fig. 4. **Our method produces more uniform radiation patterns for active sound objects and eliminates spurious high-frequency artifacts and noise in the scattering response for passive sound objects:** Our method (Bottom row) outperforms the popular staircasing approximation (Top row) for embedding objects onto the simulation grid. Red represents positive pressure, blue represents negative pressure, and white represents the embedded object. (a) spherical monopole sound source radiating well below the grid resolution limit at 3.4 kHz; (b) spherical monopole sound source radiating at the grid resolution at 8.7 kHz (our method produces a more uniform sound field); (c) passive plate scatterer; (d) passive sphere scatterer.
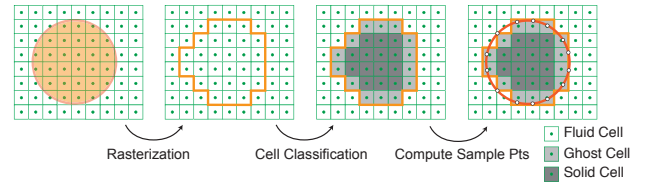

Fig. 5. **Building the simulation grid topology.** Our method starts by rasterizing the interfaces to the simulation grid and identifying a set of solid cells. Among these solid cells, those that have at least one neighbouring fluid cell are classified as *ghost cells*, which will be used to compute and store boundary condition data.

At every step, the interface is first rasterized to the grid and a set of *ghost cells*, $\{x_g\}$, are located to store the BCs (see Figure 5). The observation is that if we assign pressure values to these cells, $\{p_g\}$, then we can carry out FDTD timestepping (3) normally as if there are no objects or interfaces. The boundary effects are therefore *immersed* in the grid. For each ghost cell x_g, we first find a boundary point $x_b \in \Gamma$ closest to x_g, and then approximate the Neumann boundary condition (2) using 2nd-order centered differencing

$$\frac{p_r - p_g}{l} = -\rho a_n(x_b, t) + O(l^2), \quad (6)$$

where $p_r = p(x_r, t)$, $p_g = p(x_g, t)$, $l = |x_r - x_g|$, and x_r is the reflection point, defined by $x_r = x_g + 2(x_b - x_g)$. See Figure 6 for an illustration. We sample a_n from the corresponding sound source using acoustic shaders, which will be explained in §4. The pressure at the reflection point, p_r, is estimated using trilinear interpolation over the surrounding 8 cells. For the derivation below, we use Ω_r to denote this cubic region where the interpolant is valid.
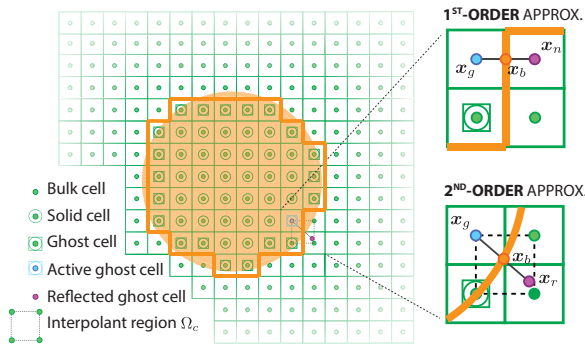
Fig. 6. Ghost cell reflection: To find the reflection of a ghost cell located at x_g, we first find a surface boundary point x_b closest to x_g, then construct a reflection stencil to impose the Neumann boundary condition. x_b can be found efficiently using spatial acceleration data structures (we used KD-tree for rigid interfaces and spatial hashing for deformable interfaces).

Since trilinear interpolation can involve other unknown ghost cells, estimating ghost-cell pressures will, in general, require solving a sparse linear system. We now describe how to construct this system. Let

$$p(x) = \phi(x) \cdot c, \quad x \in \Omega_r, \tag{7}$$

represent trilinear interpolation, with some unknown coefficients $c \in \mathbb{R}^8$, and the polynomial basis row vector $\phi : \mathbb{R}^3 \to \mathbb{R}^8$,

$$\phi(x) = [xyz \quad xy \quad yz \quad xz \quad x \quad y \quad z \quad 1]. \tag{8}$$

Requiring the interpolant to reconstruct eight adjacent pressure samples, $p \in \mathbb{R}^8$, at the sampled cell positions, $\{x_i\}_{i=1}^8$, yields the linear system

$$\Phi c = \begin{bmatrix} \text{—} \phi_1 \text{—} \\ \text{—} \phi_2 \text{—} \\ \vdots \\ \text{—} \phi_8 \text{—} \end{bmatrix} c = p. \tag{9}$$

where $\phi_i \equiv \phi(x_i)$. When one of the interpolation stencils involves the unknown itself at x_g, degeneracy in (6) can happen as $l \to 0$ and the problem becomes singular. To avoid the singularity, we replace a row of Φ using the Neumann BC when this happens, similar to [Mittal et al. 2008]. Concretely, since x_b is guaranteed to be in Ω_r, the normal derivative of the interpolant (7) must follow the Neumann BC at x_b:

$$\partial_n p(x_b) = \partial_n \phi(x_b) \cdot c = -\rho \, a_n(x_b). \tag{10}$$

Since the only unknown in this equation is c, we can use this relationship to replace a row of the linear system in (9) without changing the interpolant. Let the jth row be the one contributed by x_g, then we replace the jth row of (9) with (10) and obtain $\tilde{\Phi} c = \tilde{p}$. We use SVD decomposition to solve the system

$$c = \tilde{\Phi}^{-1} \tilde{p}. \tag{11}$$

We can then evaluate the interpolant at x_r to get $p_r = \phi(x_r) \cdot \tilde{\Phi}^{-1} \tilde{p}$. Substituting this back to (6), we derive a scalar equation for computing the ghost cell pressure p_g.

$$p_g - \phi(x_r) \cdot \tilde{\Phi}^{-1} \tilde{p} = l\rho \, a_n(x_b, t). \tag{12}$$

Note that in general $\tilde{p}$ involves pressure values of other ghost cells, which are unknowns coupled to p_g. Applying (12) to N_g ghost pressure samples gives us a sparse linear system, $Ag = b$, where A is of size N_g-by-N_g and g is the vector of all ghost cell pressures. A is a sparse matrix (number of non-zero entries is upper bounded by $8N_g$). We solve the linear system using BiCGStab, and observe stable and fast convergence for all of our examples. Since A only depends on the position of the interfaces, it can be precomputed and cached for static scenes.

In Appendix A, we show that the interpolation matrix $\tilde{\Phi}$ can be ill-conditioned. When this occurs, the weights for the trilinear interpolation can grow unbounded and cause pressure instabilities. In our hybrid approach, we compute the condition number of $\tilde{\Phi}$ from the SVD decomposition, and aborted the high-order solve when it exceeds a user-defined threshold, κ. In this case, we directly set the reflected point to the corresponding grid-aligned neighbouring cell, $x_r \leftarrow x_n$. Equation 12 is then collapsed to the 1st-order staircasing estimator, $p_g - p_n = l\rho \, a_n(x_b, t)$. Note that $\kappa = \infty$ yields 2nd-order accuracy and $\kappa = 0$ yields 1st-order accuracy. We observed $\kappa \approx 25$ is sufficient to maintain a low replacement rate without instability; since trilinear interpolation is translation and scale-invariant, stencils in (12) are transformed to the $[-1, 1]^3$ cube before evaluation, thus permitting a constant threshold value κ for all examples. Please see Appendix C for more analysis on the accuracy of interface tracking.

3.3 Time-consistent Dynamic Interface Tracking

We now describe a method to track the pressure field with dynamically embedded interfaces, allowing plausible sounds to be produced by animations, such as the familiar spolling bowl (see Figure 7). Interface movements create discrete cell "jumps" that can cause audible pops in the generated sound if care is not taken. More specifically, when a cell transitions from a "solid" to "fluid" cell, a robust extrapolation procedure is needed to estimate the pressure history of the cell, otherwise the time-curvature estimation of the wave equation (1) will fail, and this will lead to a pressure discontinuity, and possible "pop" sound artifacts and noise. In the CFD literature, this is known as *the fresh-cell problem* [Mittal and Iaccarino 2005].

Instead of a more expensive global solve, such as in [Mittal et al. 2008], we compute the fresh-cell pressures locally. For a freshly appearing cell located at x_f, we find a closest point x_b on the boundary (with acceleration a_b) and enforce the 2nd-order Neumann boundary condition locally, i.e.,

$$p_f - p_r = -\rho \, a_b \cdot (x_f - x_r), \tag{13}$$

Here the reflection point is defined as $x_r = x_b + 2(x_f - x_b)$. We then estimate $p_r = p(x_r, t)$ using linear Moving Least Squares interpolation over valid neighboring cells, $\{p_i | i^{\text{th}}$ neighboring fluid cell$\}$. Compared to the ghost-cell solve, fresh-cell extrapolation is only needed sparsely in time and space, and we found this approximation to be sufficient to get rid of the aforementioned discontinuity (and "pop" artifacts). The process is illustrated in Figure 8.
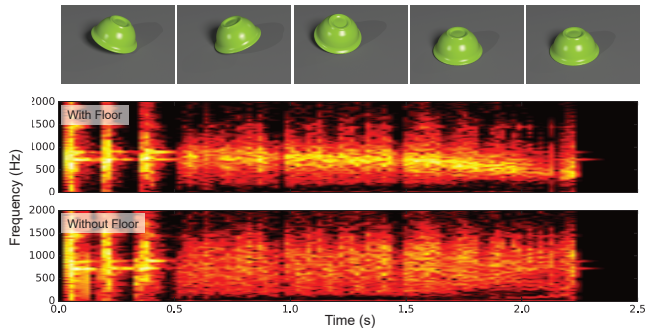
Fig. 7. **Spolling bowl**: Properly tracking dynamic interfaces and the associated pressure field allows us to simulate time-varying cavity resonance. In this case, the contact between the spinning-and-rolling bowl and the ground floor creates a Helmholtz-like resonator that has a time-varying "opening" size. Our solver is able to automatically synthesize the familiar decreasing pitch shift at the end of the motion (when the cavity closes up) without any additional modeling.
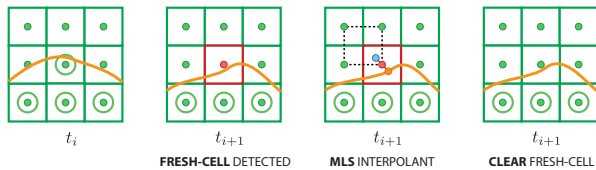

Fig. 8. **Fresh-cell problem:** When the interfaces move, cells that were previously solid cells are marked as fresh-cells, and an extrapolation procedure based on linear MLS is performed to fill the pressure history. The extrapolated pressure satisfies Neumann boundary condition on the nearest embedded interface.

We note that, although mathematically equivalent, the pressure-velocity (P-V) formulation for the acoustics wave equation used in [Allen and Raghuvanshi 2015; Chadwick et al. 2012b] is less well suited for our interface tracking method. This is because in a staggered P-V solver, pressure cells and velocity cells have an offset that is half a cell wide, and thus they can have different reflected points. After extrapolation the errors in pressure and velocity cells can be inconsistent, which causes spurious velocity divergence and artifacts in the rendered sound, and thus led to the development of our specific method.

In summary, a single solver update involves the following steps:

(1) Update the objects and interfaces according to the input animation.
(2) Voxelize the objects to the simulation grid, and identify ghost and fresh cells.
(3) Iterate through the fresh cells and perform MLS interpolation.
(4) Iterate through the ghost cells and sample acoustic shaders to construct entries of A.
(5) Solve the sparse linear system $A\boldsymbol{g} = \boldsymbol{b}$.
(6) Time-step the wave equation for all fluid cells and update the absorbing layers.

4 ACOUSTIC SOURCE SHADERS

We now describe how we model sound sources in our system. We use *acoustic shaders* as a convenient abstraction for evaluating sound

sources, notably for acceleration boundary conditions on surfaces. Each such acceleration shader component keeps any necessary internal state up-to-date with the main solver, and, when queried, provides surface acceleration data that will be used to compute the ghost cell pressures using (12).

Since the wave equation and the Neumann boundary conditions are linear, the boundary acceleration at surface position $\boldsymbol{x}_b$ is simply the sum of accelerations from all the S shaders

$$\boldsymbol{a}_b(\boldsymbol{x}_b, t) = \sum_{i=1}^{S} \boldsymbol{a}_b^i(\boldsymbol{x}_b, t) \qquad (14)$$

This allows the solver to amortize the wave propagation solve, and also reuse data that are expensive to compute across different shaders, such as the shader sampling location $\boldsymbol{x}_b$.

Below we describe a set of acoustic shaders that are implemented in our solver, and discuss shader-specific considerations regarding evaluation speed, accuracy, and efficiency.

4.1 "Canned" Sound Sources

Standard point-like or area sound sources can be used to play a pre-recorded sound at a specific location. For example, a user may desire to place an input signal $a_0(t)$ on a 3D trajectory of a point, $\boldsymbol{x}_0(t) : \mathbb{R} \to \mathbb{R}^3$. We render point-like and area-like sound sources as follows:

Point sound sources. The acoustic effect of the signal can be modeled using a point-like divergence source, $f_s = \rho \nabla \cdot \mathbb{V}_f$ for some velocity field $\mathbb{V}_f$. We modify the wave equation (1) to accommodate this term,

$$\frac{\partial^2 p(\boldsymbol{x}, t)}{\partial t^2} = c^2 \nabla^2 p(\boldsymbol{x}, t) + c\alpha \nabla^2 \frac{\partial p(\boldsymbol{x}, t)}{\partial t} + \frac{\partial f_s(\boldsymbol{x}, t)}{\partial t}, \ \boldsymbol{x} \in \Omega. \quad (15)$$

We then enforce the source on a single-cell $\boldsymbol{x}_c$, i.e., $f_s(\boldsymbol{x}_c, t) = a_0(t)$.

Area sound sources. Some sound sources are naturally modeled using a vibrating surface area, such as a small speaker on cell phone (Figure 14). In these cases we define a dynamic surface patch $\Gamma_0(t)$, and impose the Neumann boundary condition, $a_n(\boldsymbol{x}, t) = a_0(t)$, $x \in \Gamma_0(t)$ for the "canned sound can be played". Notice that assigning $a_n = 0$ is equivalent to having a perfectly reflecting boundary.

4.2 Modal Vibration Shader

The modal sound pipeline for rigid bodies is widely studied in computer animation (e.g., see [Zheng and James 2010, 2011]), and it relies on linear modal analysis, a technique commonly used to approximate small vibrations in a low-dimensional basis. Specifically, the dynamics for such objects are approximated by a set of M uncoupled oscillators reacting to external forces $f(t)$ [Shabana 2012, 2013], given by $\ddot{\boldsymbol{q}}(t) + \tilde{C}\dot{\boldsymbol{q}}(t) + \tilde{K}\boldsymbol{q}(t) = U^T f(t)$, where $\boldsymbol{q} \in \boldsymbol{R}^M$ are the modal displacements, $\tilde{C}$ and $\tilde{K}$ are the constant M-by-M reduced damping and stiffness matrices, and $U \in \boldsymbol{R}^{3N \times M}$ is the time-invariant eigenmode matrix. The solutions $\boldsymbol{q}(t)$ can be time-stepped using an unconditionally stable IIR filter [James and Pai 2002]. The displacements $\boldsymbol{u} \in \mathbb{R}^{3N}$ of an N-node object at time t can be recovered by the transformation $\boldsymbol{u}(t) = U\boldsymbol{q}(t)$. Assuming N boundary nodes/vertices, the boundary-vertex accelerations are given by $\ddot{\boldsymbol{u}}(t) = U\ddot{\boldsymbol{q}}(t)$.

The modal shader only needs to evaluate the normal component of the surface-vertex accelerations, so we precompute the matrix $U_n \in R^{N \times M}$ of the normal components of eigenmode displacements. When the surface acceleration is needed at vertex i, we evaluate (and cache) a sparse $u_i^\mathsf{T} q$ lookup, where u_i^T is the i-th row of U_n. Finally, similar modal vibration shaders can also be implemented for nonlinear reduced-order models [Chadwick et al. 2009], although the internal $\ddot{q}$ calculations would differ.

4.3 Acceleration Noise Shader

Small rigid objects can have inaudibly high modal frequencies. In such cases, the distinctive click sounds of small objects are largely due to so-called acceleration noise, due to rapid rigid-body accelerations. We implemented an acceleration noise shader based on Chadwick et al. [2012b]. The model estimates a contact timescale based on the idealized local conformal geometry and Hertz contact theory. To ensure consistency, we enforce the same contact timescale model for both the modal and acceleration noise shader, as they often appear together. However, we do not implement their precomputation-based pipeline, but rather compute the radiation on-the-fly for specific contact-acceleration events using our pressure-based FDTD wave-solver. For more details on evaluation rigid-body accelerations for Hertz-like contact events, please see the referenced paper.

4.4 Water Bubble Shader

Langlois et al. [2016] recently used two-phase incompressible simulations of bubbly water flows to generate water sound. However, that work approximated the radiation of the bubbles through a sequence of steady-state frequency-domain Helmholtz radiation solves, which missed transient effects, such as acoustic wave interactions with the rapid time-varying shape of the water surface. We have resimulated the radiation portion of several of these examples, to demonstrate the drastic and audible differences these transient effects create.

The data from that work consists of a sequence of water surface meshes $\{m_i\}$ (sampled at 1 ms intervals) which have acoustic velocity data for each bubble (normalized for unit vibration). For bubble j at time t_i, denote this spatial velocity field as $u_i^j(x)$. The normal velocity values are stored at triangle centers. Multiplying by the bubble's volume velocity $\dot{\upsilon}_i^j$ gives the actual surface normal velocity due to bubble j at time t_i. The full acoustic surface velocity is the superposition of the velocities contributed by all n vibrating bubbles at time t_i:

$$u_i(x) = \sum_{j=1}^{n} u_i^j(x) \dot{\upsilon}_i^j \qquad (16)$$

Taking the time derivative of the normal velocity in (16) gives the normal acceleration BC needed by the water shader. However, because the water meshes are incoherent between time steps, we compute this normal acceleration using central differences. The process is illustrated in Figure 9. To spatially interpolate the velocity data between incoherent meshes, we used nearest-neighbor interpolation, which does not suffer from any conditioning problems. It is possible for topological changes to cause interpolation artifacts, but we have not observed them.
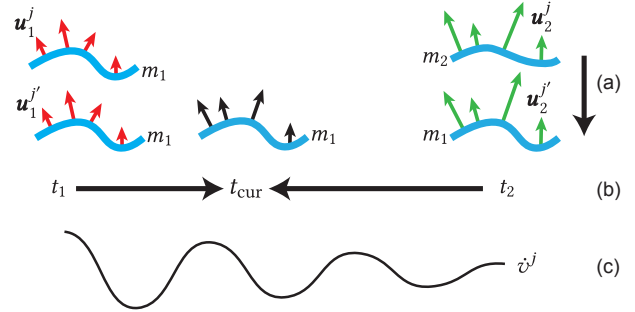

Fig. 9. **Water Shader Sampling:** When calculating the acceleration for a bubble j at time t_{cur}, we have velocity data u_1^j and u_2^j at times t_1 and t_2. To calculate the acceleration at time t_{cur}, we first (a) spatially interpolate the velocities to the same mesh. Since t_{cur} is closer to t_1 in this example, m_1 is used, and u_1^j does not require interpolation. Then (b) the velocities are linearly interpolated to the same time. Finally, (c) this velocity is multiplied by the bubble's volume velocity $\dot{\upsilon}^j$ at time t_{cur}. This process is repeated at $t_{\text{cur}} - dt$ and $t_{\text{cur}} + dt$, and a centered finite difference is used to compute the acceleration.

4.5 Finite-element Shell Shader

Nonlinear thin shells can produce sounds with complex attack/decay patterns, and are challenging due to the potential for large deformations. Because of the highly nonlinear vibrations and strong transient effects, frequency-domain solvers are not ideally suited for synthesizing shell sounds. In contrast, our time-domain wave-solver is capable of simulating thin-shell sound radiation without modifications.

We implemented a shell shader using the elastic shell model of Gingold et al. [2004]. The equation of motion is

$$\ddot{u} + D\dot{u} + f_{\text{int}}(u) = f_{\text{ext}}, \qquad (17)$$

where the nonlinear internal force, f_{int} includes contributions from membrane forces that penalize stretching and compression, and bending forces that penalize bending away from the rest configuration. Time-stepping these equations using, e.g., explicit or implicit Newmark, one can obtain the normal vertex accelerations, For more details, please see [Chadwick et al. 2009; Gingold et al. 2004].

However, thin shells are more difficult to robustly rasterize and sample from. To ensure the shells are properly resolved, we use a triangle-cube rasterizer based on [Akenine-Möller 2002]. However, naïvely doing so at every timestep incurs a high quadratic cost. Instead, we impose an additional CFL condition for the shell object such that each vertex can travel at most 1 grid cell at a given time step. Then we can use this to bound the object motion, which minimizes the search range (see Figure 10). This relatively simple optimization reduces the cost of rasterization in our system by $2-5x$.

Thin shells also pose challenges in finding valid reflection points for the ghost-cell method. For shells, it is possible to have interpolation stencils cross the discontinuous interface. In practice, these cases can cause pressure leakage and artifacts in the rendered sound. This artifact is preventable but the solution often comes with high overhead (such as doing ray-tracing when establishing reflection). Therefore, for shells, we currently set the ghost-cell solve condition number threshold to $\kappa = 0$, enforcing the solver to always run
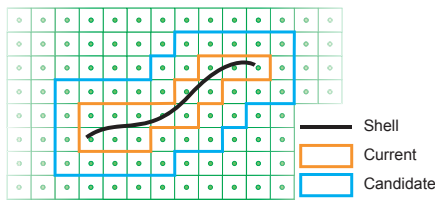
Fig. 10. **Optimization for rasterizing thin shells**: Because the shell motion is much slower than the speed of sound, we can freely enforce an object-CFL condition such that any point on the shell cannot move more than one cell per step. This greatly reduces the number of candidate cells that need to be checked in the next time step for rasterization, which is a slow, quadratic-complexity operation.

the staircasing boundary handling for maximized robustness, albeit with slightly noisier sound synthesis.

5 ESTIMATION OF RADIATED SOUND

Since time-domain wave synthesis is expensive, we only simulate pressure waves in a small region about each sound source, and estimate the far-field pressure signal using multiple sample points along an outgoing-ray delay line similar to Chadwick et al. [2012b]. Specifically, for each listening position x_l, we construct a line connecting the simulation box center y and x_l. We obtain the pressure time series $\{p_i\}$ for a set of points $\{x_i\}$ along each delay line. Along this ray, outside the source region, the far-field pressure is assumed to follow a K-term radial function expansion, similar to [Chadwick et al. 2012b] (and motivated by the Atkinson-Wilcox theorem [Marburg and Nolte 2008]):

$$p(\boldsymbol{x}, \tau) \approx \sum_{j=1}^{K} \frac{\alpha_j(\tau)}{r^j}, \qquad (18)$$

where $r = \|\boldsymbol{x} - \boldsymbol{y}\|$, and for samples of a constant phase $\tau = t - r/c$. The coefficients $\alpha_j(\tau)$ are estimated from $\{(r_i, p_i)\}$ using a least-squares fit. In our examples, we often just use a single-point pressure sample (r_1, p_1) ("close mic'ing") to provide the simple estimate $p(r, \tau) \approx \frac{r_1}{r} p_1(\tau)$. One limitation of this approach is that near-field non-radiating evanescent waves can be artificially amplified, e.g., if one placed a microphone very near to a pair of headphones to get an estimate of the far-field sound it would overestimate the low-frequency content.

Discussion. While we use simple single- or few-point pressure estimators in our examples, we note that the full Kirchhoff-Helmholtz integral [Botteldooren 1997] can give a more accurate result. However, that requires evaluting a computationally expensive space-time integral, and is sensitive to numerical dispersion errors [Bilbao 2009; Botteldooren 1997]. Instead, our reconstruction method is simple, and trivial to evaluate.

6 TIME-PARALLEL SOUND SYNTHESIS

Parallelization of FDTD codes usually relies on efficient multi-threading of finite-difference stencil computations within each timestep [Micikevicius 2009]. Unfortunately, for sound synthesis we can have relatively modest spatial domains (e.g., 80^3 cells), but millions of sequential timesteps, which limits parallelization. Fortunately, we

have developed a simple time-parallel sound synthesis method that is complementary to fine-grained multi-threaded computing, and is pleasantly parallel and amenable to cloud computing.

Time-Parallel Method. The key to our approach is to observe that most sound sources tend to have short acoustic response times: waves emitted due to a brief source event typically bounce around briefly before leaving the sound region, and subsequently eliminated by an absorbing boundary condition or perfectly matched layer. The other key observation is that the resulting sound waveform, p, is linearly dependent on the space-time BC acceleration data, a, by linearity of the wave-equation solution operator, $p = \mathcal{W}a$. Therefore, by the linear superposition principle, if we temporally partition all BC data using a box (or other) filter into N_c "chunks,"

$$a(\boldsymbol{x}, t) = \sum_{i=1}^{N_c} a_i(\boldsymbol{x}, t), \qquad (19)$$

then the pressure resulting from $a(\boldsymbol{x}, t)$ is simply

$$p(\boldsymbol{x}, t) = \sum_{i=1}^{N_c} p_i(\boldsymbol{x}, t), \qquad (20)$$

where $p_i = \mathcal{W}a_i$ is the solution to $a_i(\boldsymbol{x}, t)$ BC data. Please see Figure 11 for an illustration of this process.
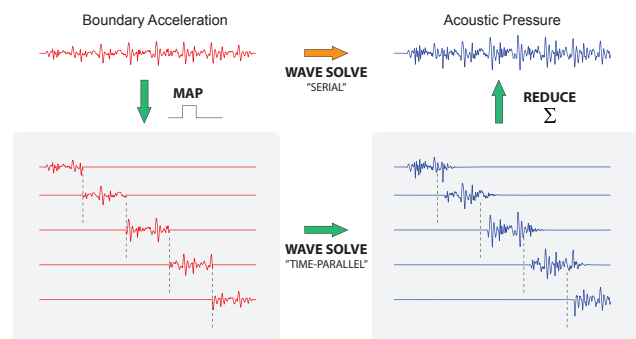

Fig. 11. **Time-Parallel Sound Synthesis:** The input acoustic shader data is first temporally partitioned into a set of non-overlapping chunks. We then launch wave solvers in parallel for all the chunks for the nonzero duration of the shader data, plus a small overlap time. The computed pressures are then gathered and summed to obtain the full pressure. Our algorithm adaptively determines each chunk's overlap time by monitoring the listener pressure output. (The waveforms shown are actual data from the "Trumpet" example.)

We use a box filter so that $\{a_i(\boldsymbol{x}, t)\}$ are temporally maximally disjoint functions. However, the partial wave solutions p_i will not be disjoint in time, and can exhibit varying decay rates. Therefore if T_i^0 is the duration of the windowed support of $a_i(\boldsymbol{x}, t)$ in time, then we run the wave solver for time $T_i = T_i^0 + \epsilon_i$, where ϵ_i is a small overlap time that allows (resonating) waves in the domain to die out. In practice each chunk's wave solution p_i need only be simulated in a small window about the nonzero a_i BC data. Since there is no communication between chunks, the synthesis problems are pleasantly time parallel.

Table 1. **Statistics**: We report the duration of each example, the cell size, the number of cells along each dimension (cubic domains), the number of steps per second, total number of steps, wall clock runtime, and number of CPU cores used. Solver runtimes do not include any physics-based simulation required for shaders, but may involve simulation data I/O.

Example	Duration (s)	Cell Size (mm)	Grid Dim	Step Rate (kHz)	Total # Steps	Runtime	# Cores
Dripping Faucet	8.5	5	80	192	1600 k	18.6 hr	32
Pouring Faucet	8.5	5	80	192	1600 k	55 hr	64
Blue LEGO Drop	0.21	1	50	615	130 k	32 min	320
Spolling Bowl	2.5	5	50	120	300 k	63 min	256
Bowl and Speaker	9	7	39	88.2	790 k	45 min	320
Wineglass Tap #5	1	5	54	120	120 k	50 min	36
Cymbal	5	10	80	88.2	440 k	65 min	640
Metal Sheet Shake	10	14.3	99	44.1	440 k	24 hr	36
ABCD	5	5	80	119	590 k	43−69 min	256
Cup Phone	8	7	90	88.2	710 k	41 min	640
Talk Fan	10.5	10	85	88.2	930 k	67 min	640
Trumpet	11	10	70	88.2	970 k	33 min	640

Adaptive Overlap Time. The overlap time for each chunk, ϵ_i, is determined adaptively by thresholding the observed pressure values at the listener locations, x_l. Note that the waves are oscillatory, so we monitor recent pressure values until they fall below a threshold; in our implementation, we use a fixed window size of $t_w = 50$ ms (20 Hz). We start checking this termination criteria when there is no nonzero acceleration data. We terminate the ith solver at time t^* if

$$\frac{\max_{t \in \tilde{T}} |p_i(x_l, t)|}{\max_{t \in T} |p_i(x_l, t)|} < \delta_{\text{rel}} \quad \text{or} \quad \max_{t \in \tilde{T}} |p_i(x_l, t)| < \delta_{\text{abs}},$$

where $T = [0, t^*]$ and $\tilde{T} = [t^* - t_w, t^*]$. We use $\delta_{\text{rel}} = 0.001$ and $\delta_{\text{abs}} = 20 \, \mu\text{Pa}$ for our examples.

Adaptive Chunk Partitioning. Many of our shaders can have sparse acceleration data, such as the acceleration noise shader and the 3D re-recording shader. Instead of time-stepping a lot of (near) zero values, we can further reduce costs by adaptively selecting chunk partitions to avoid zeros. In our implementation, we divide nonzero BC data into uniform chunks, trimming chunks to avoid unnecessary front/end zero data. We can uniformly or adaptively subdivide until we obtain the desired number of chunks, or a minimum chunk duration, is achieved.

7 RESULTS

We now present a variety of animation-sound results that were synthesized using the same FDTD wave-solver pipeline with different acoustic shaders. These results demonstrate the ability of our method to synthesize challenging new phenomena, as well as to reproduce existing phenomena. Several technical validations and tests of our algorithms and implementation are also provided. We strongly encourage readers to view all of our audiovisual results in the accompanying video.

7.1 Implementation Details

Our system is implemented in C++, and evaluated on a variety of Intel multi-core processors using a multi-threaded implementation.

Additionally, large sound examples were rendered on the Google Cloud Compute platform by exploiting our time-parallel method (§6). Table 1 reports statistics and performance for all the examples presented. We used libigl [Jacobson et al. 2017] for geometry processing such as curvature computation and Eigen [Guennebaud et al. 2010] for linear algebra operations.

7.1.1 Discretization Criteria. We now discuss the discretization criteria used to initialize the simulation grid, and select the cell size, h. In general, we tried to minimize the solve time while preserving important geometric features of our models (e.g., LEGOs have small resonating cavities at the back). For our examples, we follow the guidelines below for selecting the discretization: (1) the grid dimension and the center are chosen to cover the minimal volume for each example within a given time partition; (2) the cell size is chosen fine enough to preserve important geometric features (such as the thin wall of the LEGOs), while being as coarse as possible to reduce runtime. There are additional cell size selection criteria, notably the wavelength sampling criterion (heuristically the grid should have more than $4 - 5$ cells per wavelength of interest). However, we found that (2) is typically stricter than these criteria for selecting cell size and thus they are not explicitly enforced.

Since our focus is on near-field effects, the region-of-interest for our examples are relatively well-contained spatially (see Table 1), which in turn means that the numerical dispersion errors that might trouble long-range FDTD simulation [Saarelma et al. 2016] are practically non-existent in our case. Please see Figure 12 for justification of this claim.

7.1.2 Rough Floor Modeling. Abrupt grid topology changes can cause unwanted sound effects. For example, at the end of the spolling bowl movement the resonant cavity becomes completely sealed, which can cause an artificially sharp amplitude drop. Although this unwanted effect can be mitigated using smaller cell sizes (to resolve smaller gaps between the bowl and the floor), they incur
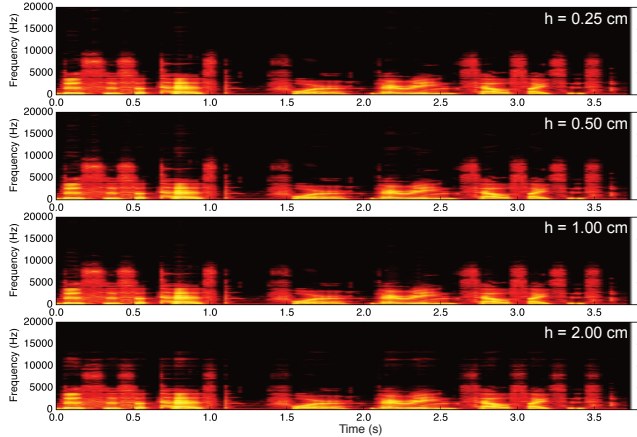
Fig. 12. **Effect of cell sizes on a complex speech example**: In this example, we uniformly shaded a sphere with area re-recording shader with the dialogue "This is a test on varying cell sizes" (bandlimited to 10 kHz), and ran the simulation using different cell sizes. The spectrograms are almost identical, except for $h = 2.00$ cm, where slight low-pass effects can be seen due to the undersampling of the highest frequencies (for example, 10 kHz has only ≈ 1.7 sample points per waveform for this grid). Please see the supplemental material for the audio samples.

a significant cost. Instead, we introduced patterned floor grooves and holes in the rasterization cavity (see Figure 13). In addition, this simple trick allows us to hear the music in the speaker-bowl example (Figure 19), even though two-way solid-fluid coupling is not modeled. This floor geometry is used in the LEGO and the spolling bowl example; otherwise our floor geometry matches the rendered geometry.
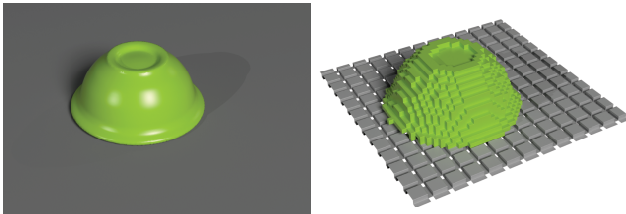

Fig. 13. **Rough floor modeling**: Unwanted artifacts can arise from the abrupt cavity closure at the end of the spolling bowl movement. To prevent these artifacts, we crosshatched 1-cell grooves on the floor spaced every 4 cells in each direction, and we drilled a 4×4 pattern of 1-cell holes into the surface. (Right) A visualization of the solid cells in the simulation.

7.2 3D Re-recording

3D re-recording is an effective demonstration of the FDTD solver's ability to handle dynamic interfaces when sound sources (point- or area-like) are placed near animated scene geometry. We explore 3D re-recording for generic animated scenes and virtual characters.

Kinematic Deformers. We present several examples of sound sources placed into keyframed animations for the purpose of 3D re-recording. The synthesized sounds naturally vary with changes in the dynamic

3D scene. Several examples include the ringing phone example (see Figure 14) and those in Figure 16.

Fig. 14. **Area source 3D re-recording shader.** For a directional sound source, the user inputs a surface patch they want to apply the source on. We then directly specify the Neumann boundary condition. In this example, we attached two rectangular patches at the bottom of the phone and play the familiar "marimba" ringtone.

Characters: 3D automatic dialogue replacement (3DADR). We develop a new method to perform 3D automatic dialogue replacement (3DADR) for virtual characters (see Figure 15). ADR is the traditional process by which actors re-record dialogue after the filming process to improve audio quality or reflect dialogue changes. Using our general-purpose wavesolver, we can enhance this process by automatically processing the character dialogue to include the physical effects of character movement and dynamic nearby scene geometry. In our implementation, we input recorded dialogue as a (dynamic) point or area sound source in the 3D scene, then re-render the final sound. Since these examples do not involve any (inherently serial) simulation of physics-based dynamics and have minimal I/O (only keyframes information is needed), they are particularly amenable to efficient computation using time-parallel cloud computing.

7.3 Water

We resynthesized sound using the geometry and vibration data from [Langlois et al. 2016], as shown earlier in Figure 2. Our synthesized water sounds show stark differences from those generated using the original, frequency-based acoustic transfer pipeline in [Langlois et al. 2016]. We use their exponential extension, but not microbubbles or their popping model. In our acoustic shader implementation, when bubbles disappear before their oscillation is finished, we continue interpolating their last valid velocity data to the current wavesolver geometry, and the oscillator is extended with the exponential function from [Langlois et al. 2016].

The FDTD solver captures more interesting bubble-based sounds, as demonstrated by a single bubble from the dripping faucet example, where container resonances can be seen (and heard) (see Figure 17). Whereas the previous method could only provide frequency-dependent amplification of each bubble oscillator, our approach simulates a fuller spectrum and sustains resonances at other frequencies. The difference in the pouring faucet example (see Figure 2) is striking. The spectrogram shows extra high frequency content. Qualitatively,
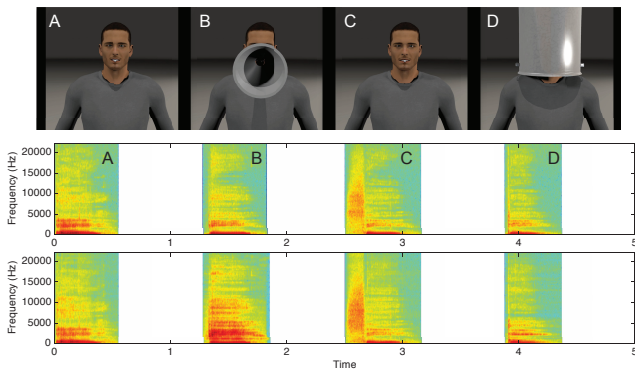
Fig. 15. **Application: 3D Automatic Dialogue Replacement (3DADR)**: Our system can perform automatic auralization for dialogue placed in 3D scene. In this example, user specifies a wav file containing a dialogue saying "A B C D" (Top row), along with a silent, dynamic 3D scene. By shading the mouth part of the character with the area source shader, our solver *renders* the audio scene and produces a plausible, automatically enhanced dialogue (Bottom row). Corresponding to the visual events, the overall sound magnitude for "B" (megaphone) is boosted (megaphone), and certain (resonance) frequencies for "D" (soup pot) are emphasized.

the wavesolver produces a more realistic "wet" sound, compared to the previous method which essentially played underwater bubble sounds with adjusted amplitudes. Ironically, *our wavesolver is faster* than the radiation solves in the previous frequency-domain approach, because the bubbles' contributions are amortized to one wave solve pass.

7.4 Rigid-body Sound

Comparison to "Acoustic Transfer" (Wine glass). The frequency-domain Helmholtz radiation is known to be a good approximation in certain cases, such as isolated objects in free-space. We compare impulse responses of a suspended wine glass (see Figure 18) between our time-domain method and the frequency-domain method in [Langlois et al. 2014], and obtain very similar impulse responses.

Time-varying acoustic interactions (Spolling Bowl, LEGO). Dynamic inter-object interactions cannot be accounted for using the single-object, precomputed Helmholtz acoustic transfer model, widely used in previous work [Zheng and James 2011]. On the contrary, our method captures several interesting and perceptually important near-field effects such as the time-varying resonance caused by a spolling bowl on the ground (see Figure 7), or the distinctive sound that LEGO pieces make when landing on different sides (see Figure 20).

Integrated multi-shader support (Bowl covering speaker). The acoustic shader abstraction provides a natural mechanism for combining different types of shader models. Please see Figure 19 for an example that demonstrates the multi-shader support (spolling bowl over speaker). Simultaneously simulating the 3D re-recording, modal, and acceleration shaders allows us to capture perceptually important near-field acoustic effects.

7.5 Thin Shells

It is straightforward for our system to support dynamic interfaces arising from unreduced discrete deformable models, e.g., standard FEM models. To demonstrate this, we synthesized nonlinear thin-shell sounds from (1) the rapid deformation of *crash cymbals* after being hit by a drumstick, and (2) a *rectangular metal plate* subjected to large bending and twisting motions (see Figure 21). Spectrogram analysis shows that these sounds are extremely broadband and experience complex pitch shifts and spectral cascades throughout the animation. Previous methods based on linear modal transfer such as [Chadwick et al. 2009] will most certainly fail under these extreme cases due to the frequency-localized transfer approximation. These basic "sheet metal" examples illustrate our system's ability to synthesize sound for general large-deformation discrete deformable models, as opposed to reduced-order modeling [Chadwick et al. 2009]. Readers interested in more detailed, predictive modeling of cymbals and plates should refer to prior work in the computer music literature [Bilbao 2009; Chaigne et al. 2005; Ducceschi and Touzé 2015].

8 CONCLUSION AND DISCUSSION

We have explored high-quality offline wave-based sound synthesis for computer animation using a prototype CPU-based FDTD implementation, with dynamic embedded interfaces and animation-based acoustic shaders. While the simulations are unoptimized and expensive, they demonstrate that a rich variety of high-fidelity sound effects, some never before heard, can be generated. Perhaps the most significant improvements are in complex nonlinear phenomena, such as bubble-based water, where no prior methods can effectively resolve the complex acoustic emissions. Our proposed parallel-in-time sound-synthesis methods were effective at exposing additional parallelism for CPU-based cloud computing, and worked especially well for 3D re-recording examples where data transfer costs were minimal. We believe this work demonstrates that future integrated high-quality animation-sound rendering systems are indeed plausible, and closer than ever before.

Given the exploratory nature of this work, there are many lessons learned, many limitations exposed, and many opportunities for future work. The most obvious limitation of our approach is that it is slow. Our CPU-based prototype allowed us to explore the numerical methods needed to support general animated phenomena, but the sound system "screams out" for GPU acceleration, so well leveraged by prior FDTD sound works [Allen and Raghuvanshi 2015; Webb 2014]. Unique challenges for GPU acceleration here are supporting dynamic embedded interfaces, and physics-based acoustic shader implementations and/or data transfer of audio-rate boundary data. Future pipelines would greatly benefit from simultaneous animation/sound synthesis, to avoid excessive data storage and transfer. Parallel-in-time sound methods can greatly improve the parallelization of long sound synthesis jobs, such as in feature production, and are well suited to multi-GPU architectures. They might also be explored for dynamics to alleviate bottlenecks and data transfer. Parallel-in-time methods are less effective for short clips, and sound sources with long reverberation times.
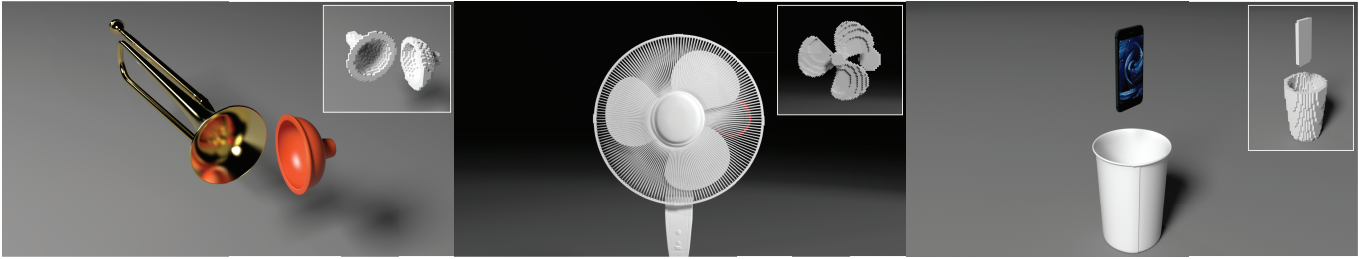
Fig. 16. **Kinematic Deformers**: The objects in all three scenes are kinematically scripted in Blender. They are keyframed and exported to our wavesolver to perform the 3D re-recording. (Left) The trumpet sound is pre-recorded and is auralized by the bell and the plunger silencer. The amplitude modulation due to the plunger motion can be clearly heard. (Middle) Speaker behind a rotating fan produces the familiar, funny "robotic" voice. This example also demonstrates our system is robust under rapid interface movements. (Right) Dipping your phone into a coffee cup while its ringing is not recommended, but it will change the ringtone quality to include the air resonance of the cup, depending on the height, width, and other cup geometry. These effects are captured naturally with our solver. Note that slightly simplified geometric models were used to simulate kinematic deformers: only the bell for the trumpet is simulated, and the outer casing of the fan is neglected (see inset figures for visualization of the rasterization results).
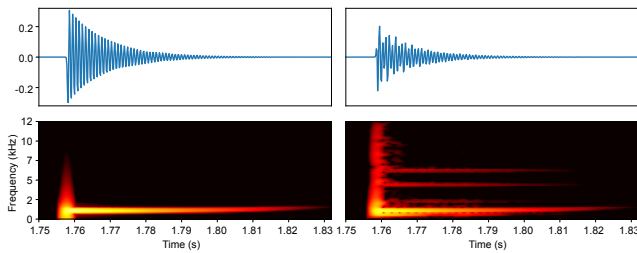

Fig. 17. **Single Bubble**: A single bubble from the dripping faucet. (Left) Results from [Langlois et al. 2016]. (Right) The same result run through our wavesolver. Note the extra container resonances excited at 4kHz and 6kHz, that the previous frequency based method could not capture.
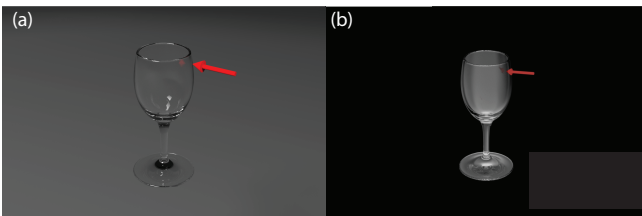

Fig. 18. **Wine glass**: Our time-domain method (a) produces similar results to the widely used frequency-domain Helmholtz radiation method (b) [Langlois et al. 2014] for the isolated wine glass in free-space.

FDTD sound synthesis for animation leads to a host of inter-related sampling and resolution issues. Low-resolution approximations can lead to rasterization errors for moving geometry and sound artifacts. Nonsmooth and under-resolved geometry can cause problems with the ghost-cell method, including inaccurate BC evaluation and even, in extreme cases, instabilities. On the other hand, using finer grids quickly gets costly: cutting spatial resolution by 1/2 in each dimension also leads to a 1/2 timestep restriction, all of which increases the cost by 16×. Our prototype uses cubic grids with a rectangular region-of-interest about each sound source, however this greatly restricts the motion of the source or can require very large domains. Future work should investigate adaptive grids, homogenization techniques to resolve multi-scale acoustics problems, and dynamically sized and moving domains for space-time adaptive computations and parallelization. Rapidly moving objects or under-sampled motions (in sample-and-hold geometry handling) can necessitate smaller timesteps, e.g., to avoid errors in fresh-cell classification which produce sound artifacts. Surface meshes must be sufficiently refined to resolve sound wavelengths of interest (typically several mm in our examples), however another problem is that very fine moving geometry can introduce aliasing artifacts when sampled on a fixed resolution FDTD grid; sampling criteria should be enforced on input geometry and BCs to ensure that such aliasing is avoided.

Computer animations can generate many challenging *near-singular and singular* acoustics scenarios. For example, sound passing through a small opening, or discontinuous changes in the acoustic domain, e.g., during contact events, can cause a click-like digital sound artifact. Contact events can lead to "closing voids" or "pinch off" events (e.g., when a bowl lands face down), and "opening voids" such as when large air bubbles burst in water animations. Without proper treatment, even very tiny voids (one to a few cells), which are easily created and destroyed, can have ill-defined discrete Laplacians for which null-space-related pressure growth can occur (due to the unconstrained velocity field) and, when the void opens, produce small clicks in extreme cases.

There are many simulation challenges and future work for sound modeling in animation. Authoring animation-sound results is difficult, and future renderers should leverage modern physics-based animation tools, like Houdini [Side Effects 2018]. Our framework uses one-way coupling, i.e., the animation drives the sound, but some systems, e.g., with enclosed air cavities like a beach ball, require solid-air coupling to properly resolve sounds. Audio-rate vibration modeling can be challenging for traditional graphics simulators not designed to resolve acoustic content; implicit integrators for deformable models can fail to converge, or produce audible artifacts when resorting to adaptive step sizes. Reduced-order vibration models, such as linear modal models, are traditionally very fast for sound synthesis, but have unique challenges for FDTD synthesis: evaluating surface acceleration BCs requires evaluating the modal transformation every timestep, which can be expensive for larger
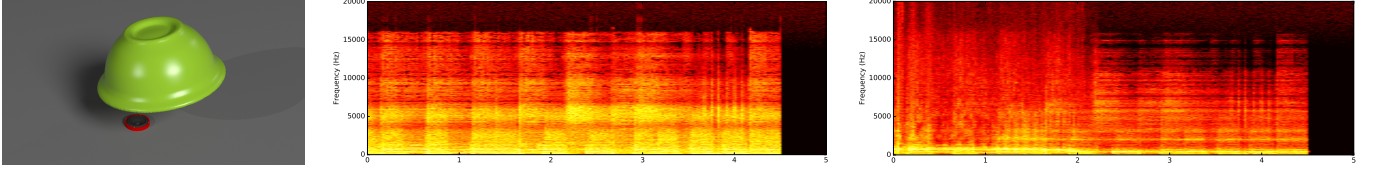
Fig. 19. **Spolling Bowl Covering a Speaker**: This example demonstrates three simultaneous acoustic shaders: 3D re-recording, modal vibration, and acceleration noise. Spectrograms of music rendered from the speaker are shown for the case of (Middle) no bowl present, and (Right) the spolling bowl on top of the speaker. The spolling bowl captures the characteristic pitch-shifting Helmholtz resonance effect. (Note: The input recording is bandlimited to 15 kHz.)

Fig. 20. **The familiar sound of LEGO**: Our system can resolve the small acoustic cavities of LEGO pieces, and even the audible orientation-dependent contact sounds when they land face-down or up (c.f. [Langlois and James 2014]).
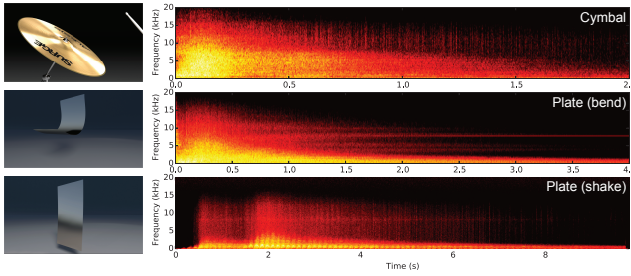

Fig. 21. **Cymbal and Plate**: Our fully unreduced nonlinear shell model results in a broadband sound for both the cymbal and the rectangular plate. (Top) The drumstick motion is kinematically scripted and it interacts with the cymbal with a linear penalty force to prevent interpenetration. The cymbal is held in place by soft spring-damper constraints which mimic the felt. The cymbal has material parameters identical to [Chadwick et al. 2009]. (Middle/Bottom) The rectangular plate is bent and shaken in two different instances. The bending motion is induced by imposing position constraints on the bottom row of vertices, which follows a circular arc. The shaking motion is done by constraining the top row of vertices, which follows a scripted shake signal. In both cases, we observe rich spectrum and complex transients in the output sounds.

objects. We have not explored acoustically transparent and absorptive media, such as cloth and fabric, but these can be important, e.g., for characters. Rapidly moving characters present challenges with diverse body poses and motions, and dynamic domains. Phenomena such as paper crumpling, fracture, vocalization, and complex machinery are exciting areas to explore.

A INTERPOLATION MATRIX CONDITIONING

We now show that the trilinear interpolation matrix, $\tilde{\Phi}$, used in the ghost-cell method can be ill-conditioned under certain circumstances. This problem is easier to illustrate in 2D than in 3D, and it generalizes to 3D (although the explicit formula for when it becomes ill-conditioned is less compact).

Consider a canonical cube C occupying the space $[0, 1]^3$. Suppose there are some data $\boldsymbol{p} \in \mathbb{R}^4$ defined over the vertices of C. The trilinear interpolant inside C can be represented with the interpolation matrix, Φ, such that for some weights $\boldsymbol{c} \in \mathbb{R}^4$, we have

$$\Phi \boldsymbol{c} = \begin{bmatrix} \text{---}\boldsymbol{\phi}_1\text{---} \\ \text{---}\boldsymbol{\phi}_2\text{---} \\ \text{---}\boldsymbol{\phi}_3\text{---} \\ \text{---}\boldsymbol{\phi}_4\text{---} \end{bmatrix} \boldsymbol{c} = \boldsymbol{p}, \tag{21}$$

where $\boldsymbol{\phi}_i = [x_i y_i \ x_i \ y_i \ 1]$ is the polynomial basis evaluated at point $\boldsymbol{x}_i$ in 2D. Suppose one of the stencils involves the ghost-cell itself and a row of Φ needs to be replaced (see §3.2). Without loss of generality, let us assume the replacement happens at the first row, where $x_1 = [0, 0]$. For a boundary point $\boldsymbol{x}_b = [x, y]$ with normal $\boldsymbol{n}_b = [n_x, n_y]$, the interpolation matrix becomes

$$\tilde{\Phi} = \begin{bmatrix} x n_y + y n_x & n_x & n_y & 0 \\ 0 & 1 & 0 & 1 \\ 1 & 1 & 1 & 1 \\ 0 & 0 & 1 & 1 \end{bmatrix} \tag{22}$$

Note that this matrix is rank-deficient when $[x, y] = [0, 0]$, and $[n_x, n_y] = [1, -1]$. Therefore, the matrix can become ill-conditioned when the boundary point gets closer to the ghost cell, and the normal is pointing near the $[1, -1]$ direction. We can observe similar behavior in 3D.

B ENGQUIST-MAJDA ABSORBING BOUNDARY CONDITIONS

The Engquist-Majda absorbing boundary condition (EM-ABC) is defined by a sequence of differential equations that are enforced at the grid boundary [Engquist and Majda 1977] in order of increasing numerical accuracy. Since the problem is symmetric in all directions, we only derive the discretization at the positive x face of the grid. We also assume no air viscosity damping $\alpha = 0$ in this derivation.

The continuous form of the 2nd-order EM-ABCs are written as

$$\frac{\partial^2 p(\boldsymbol{x}, t)}{\partial t^2} + c \frac{\partial p(\boldsymbol{x}, t)}{\partial x \partial t} - \frac{c^2}{2} \left(\frac{\partial^2 p(\boldsymbol{x}, t)}{\partial y^2} + \frac{\partial^2 p(\boldsymbol{x}, t)}{\partial z^2} \right) = 0, \tag{23}$$

where the discretized version is given by

$$\frac{p_{i,j,k}^{n+1} + p_{i,j,k}^{n-1} - 2p_{i,j,k}^n}{\tau^2} + \frac{c}{2h}(p_{i+1,j,k}^n - p_{i+1,j,k}^{n-1} - p_{i-1,j,k}^n + p_{i-1,j,k}^{n-1}) \tag{24}$$
$$- \frac{c^2}{2h^2}(p_{i,j+1,k}^n + p_{i,j-1,k}^n + p_{i,j,k+1}^n + p_{i,j,k-1}^n - 4p_{i,j,k}^n) = 0.$$

Enforcing the above equations and the FDTD discretization (3) at the boundary cell, there are two unknown pressures that can be solved for: the value at the next timestep, $p_{i,j,k}^{n+1}$, and the value in the ABC layer, $p_{i+1,j,k}^{n}$. The solutions are:

$$p_{i,j,k}^{n+1} = \frac{\lambda^2}{1+2\lambda} \left[(\frac{2}{\lambda^2} + \frac{4}{\lambda} - 6 - 4\lambda) p_{i,j,k}^{n} - (\frac{1}{\lambda^2} + \frac{2}{\lambda}) p_{i,j,k}^{n-1} + p_{i+1,j,k}^{n-1} - p_{i-1,j,k}^{n-1} \right.$$
$$\left. + 2p_{i-1,j,k}^{n} + (1+\lambda)(p_{i,j+1,k}^{n} + p_{i,j-1,k}^{n} + p_{i,j,k+1}^{n} + p_{i,j,k-1}^{n}) \right] \quad (25)$$

$$p_{i+1,j,k}^{n} = p_{i+1,j,k}^{n-1} + p_{i-1,j,k}^{n} - p_{i-1,j,k}^{n-1} - \frac{2}{\lambda}(p_{i,j,k}^{n+1} + p_{i,j,k}^{n-1} - 2p_{i,j,k}^{n}) \quad (26)$$
$$+ \lambda(p_{i,j+1,k}^{n} + p_{i,j-1,k}^{n} + p_{i,j,k+1}^{n} + p_{i,j,k-1}^{n} - 4p_{i,j,k}^{n}).$$

Here λ is a non-dimensional number defined as $\lambda = c\tau/h$. Derivations for the edges (boundaries at two directions) and corners (boundaries at all directions) are similar except there are more algebraic equations coupled. Note that the layer is 1-cell wide, since the update requires the time-history of solutions at the ABC layer.

C ACCURACY OF INTERFACE TRACKING METHOD

Figure 22 shows the error convergence between the proposed sharp-interface method and the staircasing method for handling Neumann boundary conditions. The steep cost ($\propto 1/h^4$) for reducing the cell size makes the proposed method competitive when comparing the speed-accuracy trade-off. For example, to achieve the same relative error at 10^{-2}, the proposed method requires $h = 0.005$ m and the staircasing method requires $h = 0.00125$ m, which means roughly a 256 times performance difference when max step size is taken. Figure 23 shows that for more complex example (trumpet), this extra accuracy leads to more clearly resolved high-frequency content.
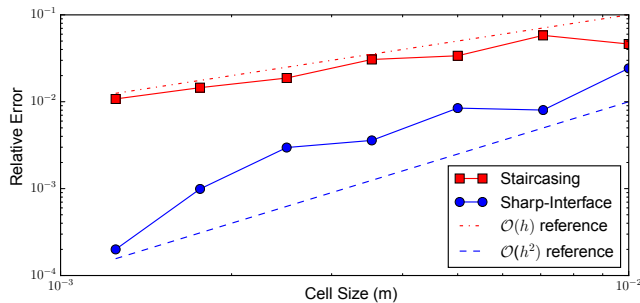

Fig. 22. **Error Analysis:** We compare our methods to the analytically derived solution for a sphere pulsating at 686 Hz. The sphere is positioned at the origin and has a diameter of 0.1 m; the simulation domain size is 0.7 m and the listening point is positioned at $[0.2, 0.0, 0.0]$ m. The proposed sharp-interface method (see §3.2) results in less error and faster convergence compared to the traditional staircasing method.
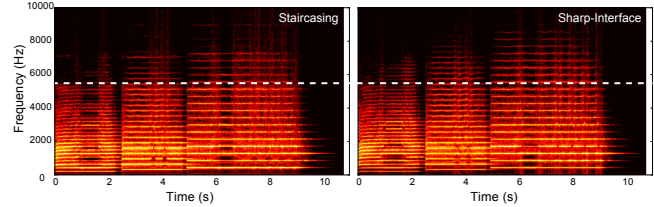
ACKNOWLEDGMENTS

Fig. 23. **Accuracy Comparison (Trumpet):** The trumpet example was simulated using (Left) a staircasing and (Right) our sharp-interface approximation, both on an $h = 0.1$ m grid. The white dashed line indicates the boundary resolution frequency (at 6 points per wavelength) for this grid. Observe that sound from the sharp-interface approximation has more high-frequency energy and sounded fuller (please refer to the supplemental material).

REFERENCES

T. Akenine-Möller. 2002. Fast 3D Triangle-box Overlap Testing. *J. Graph. Tools* 6, 1 (2002).

A. Allen and N. Raghuvanshi. 2015. Aerophones in Flatland: Interactive Wave Simulation of Wind Instruments. *ACM Transactions on Graphics (Proceedings of SIGGRAPH 2015)* 34, 4 (Aug. 2015).

S. S. An, D. L. James, and S. Marschner. 2012. Motion-driven Concatenative Synthesis of Cloth Sounds. *ACM Transactions on Graphics (SIGGRAPH 2012)* (Aug. 2012).

Avid Technology. 2018. Pro Tools. (2018). http://www.avid.com/pro-tools.

D. R. Begault. 1994. *3-D Sound for Virtual Reality and Multimedia.* Academic Press Professional, Cambridge, MA.

S. Bilbao. 2009. *Numerical Sound Synthesis: Finite Difference Schemes and Simulation in Musical Acoustics.* John Wiley and Sons.

S. Bilbao. 2011. Time domain simulation and sound synthesis for the snare drum. *J. Acoust. Soc. Am.* 131, 1 (2011).

Stefan Bilbao. 2013. Modeling of complex geometries and boundary conditions in finite different/finite volume time domain room acoustics simulation. *IEEE Transactions on Audio, Speech, and Language Processing* 21 (2013).

S. Bilbao and C. J. Webb. 2013. Physical modeling of timpani drums in 3D on GPGPUs. *Journal of the Audio Engineering Society* 61, 10 (2013), 737–748.

N. Bonneel, G. Drettakis, N. Tsingos, I. Viaud-Delmon, and D. James. 2008. Fast Modal Sounds with Scalable Frequency-Domain Synthesis. *ACM Transactions on Graphics* 27, 3 (Aug. 2008), 24:1–24:9.

D. Botteldooren. 1994. Acoustical finite-difference time-domain simulation in a quasi-cartesian grid. *Journal of the Acoustical Society of America* 95 (1994).

D. Botteldooren. 1997. Time-domain simulation of the influence of close barriers on sound propagation to the environment. *The Journal of the Acoustical Society of America* 101, 3 (1997), 1278–1285. https://doi.org/10.1121/1.418101

J. N. Chadwick, S. S. An, and D. L. James. 2009. Harmonic Shells: A Practical Nonlinear Sound Model for Near-Rigid Thin Shells. *ACM Transactions on Graphics* (Aug. 2009).

J. N. Chadwick and D. L. James. 2011. Animating Fire with Sound. *ACM Transactions on Graphics* 30, 4 (Aug. 2011).

J. N. Chadwick, C. Zheng, and D. L. James. 2012a. Faster Acceleration Noise for Multibody Animations using Precomputed Soundbanks. *ACM/Eurographics Symposium on Computer Animation* (2012).

J. N. Chadwick, C. Zheng, and D. L. James. 2012b. Precomputed Acceleration Noise for Improved Rigid-Body Sound. *ACM Transactions on Graphics (Proceedings of SIGGRAPH 2012)* 31, 4 (Aug. 2012).

A. Chaigne, C. Touzé, and O. Thomas. 2005. Nonlinear vibrations and chaos in gongs and cymbals. *Acoustical science and technology* 26, 5 (2005), 403–409.

A. Chandak, C. Lauterbach, M. Taylor, Z. Ren, and D. Manocha. 2008. Ad-frustum: Adaptive frustum tracing for interactive sound propagation. *IEEE Transactions on Visualization and Computer Graphics* 14, 6 (2008), 1707–1722.

G. Cirio, D. Li, E. Grinspun, Mi. A. Otaduy, and C. Zheng. 2016. Crumpling sound synthesis. *ACM Transactions on Graphics (TOG)* 35, 6 (2016), 181.

R. Clayton and B. Engquist. 1977. Absorbing boundary conditions for acoustic and elastic wave equations. *Bulletin of the Seismological Society of America* 67, 6 (1977), 1529.

M. Cook. 2015. Pixar, 'The Road to Point Reyes' and the long history of landscape in new visual technologies. (2015).

P. R. Cook. 2002. Sound Production and Modeling. *IEEE Computer Graphics & Applications* 22, 4 (July/Aug. 2002), 23–27.

R. L. Cook, L. Carpenter, and E. Catmull. 1987. The Reyes Image Rendering Architecture. In *Proceedings of the 14th Annual Conference on Computer Graphics and Interactive Techniques (SIGGRAPH '87)*. ACM, New York, NY, USA, 95–102. https://doi.org/10.1145/37401.37414

M. Ducceschi and C. Touzé. 2015. Modal approach for nonlinear vibrations of damped impacted plates: Application to sound synthesis of gongs and cymbals. *Journal of Sound and Vibration* 344 (2015), 313–331.

B. Engquist and A. Majda. 1977. Absorbing boundary conditions for numerical simulation of waves. *Proceedings of the National Academy of Sciences* 74, 5 (1977), 1765–1766.

Ronald P Fedkiw, Tariq Aslam, Barry Merriman, and Stanley Osher. 1999. A Non-oscillatory Eulerian Approach to Interfaces in Multimaterial Flows (the Ghost Fluid Method). *J. Comput. Phys.* 152, 2 (1999), 457 – 492.

T. Funkhouser, I. Carlbom, G. Elko, G. Pingali, M. Sondhi, and J. West. 1998. A Beam Tracing Approach to Acoustic Modeling for Interactive Virtual Environments. In *Proceedings of SIGGRAPH 98 (Computer Graphics Proceedings, Annual Conference Series)*. 21–32.

T. A. Funkhouser, P. Min, and I. Carlbom. 1999. Real-Time Acoustic Modeling for Distributed Virtual Environments. In *Proceedings of SIGGRAPH 99 (Computer Graphics Proceedings, Annual Conference Series)*. 365–374.

W. W. Gaver. 1993. Synthesizing auditory icons. In *Proceedings of the INTERACT'93 and CHI'93 conference on Human factors in computing systems*. ACM, 228–235.

Y. I. Gingold, A. Secord, J. Y. Han, E. Grinspun, and D. Zorin. 2004. A Discrete Model for Inelastic Deformation of Thin Shells.

G. Guennebaud, B. Jacob, et al. 2010. Eigen v3. http://eigen.tuxfamily.org. (2010).

Jon Häggblad and Björn Engquist. 2012. Consistent modeling of boundaries in acoustic finite-difference Time-domain simulations. *Journal of the Acoustical Society of America* 132 (2012).

P. S. Heckbert. 1987. Ray tracing Jell-O brand gelatin. In *ACM SIGGRAPH Computer Graphics*, Vol. 21. ACM, 73–74.

A. Jacobson, D. Panozzo, et al. 2017. libigl: A simple C++ geometry processing library. (2017). http://libigl.github.io/libigl/.

D. L. James, J. Barbic, and D. K. Pai. 2006. Precomputed Acoustic Transfer: Output-sensitive, accurate sound generation for geometrically complex vibration sources. *ACM Transactions on Graphics* 25, 3 (July 2006), 987–995.

D. L. James and D. K. Pai. 2002. DyRT: Dynamic Response Textures for Real Time Deformation Simulation with Graphics Hardware. *ACM Trans. Graph.* 21, 3 (July 2002), 582–585. https://doi.org/10.1145/566654.566621

M. Kleiner, B.-I. Dalenbäck, and P. Svensson. 1993. Auralization–An Overview. *J. Audio Engineering Society* 41 (1993), 861–861. Issue 11.

D. Komatitsch, G. Erlebacher, D. Göddeke, and D. Michéa. 2010. High-order finite-element seismic wave propagation modeling with MPI on a large GPU cluster. *Journal of computational physics* 229, 20 (2010), 7692–7714.

T. R. Langlois, S. S. An, K. K. Jin, and D. L. James. 2014. Eigenmode Compression for Modal Sound Models. *ACM Trans. Graph.* 33, 4, Article 40 (July 2014), 9 pages. https://doi.org/10.1145/2601097.2601177

T. R Langlois and D. L James. 2014. Inverse-foley animation: Synchronizing rigid-body motions to sound. *ACM Transactions on Graphics (TOG)* 33, 4 (2014), 41.

T. R. Langlois, C. Zheng, and D. L. James. 2016. Toward Animating Water with Complex Acoustic Bubbles. *ACM Trans. Graph.* 35, 4, Article 95 (July 2016), 13 pages. https://doi.org/10.1145/2897824.2925904

S. Larsson and V. Thomée. 2009. *Partial Differential Equations with Numerical Methods*. Springer.

Q.-H. Liu and J. Tao. 1997. The perfectly matched layer for acoustic waves in absorptive media. *The Journal of the Acoustical Society of America* 102, 4 (1997), 2072–2082.

S. Marburg and B. Nolte. 2008. *Computational acoustics of noise propagation in fluids: finite and boundary element methods*. Vol. 578. Springer.

R. Mehra, N. Raghuvanshi, L. Antani, A. Chandak, S. Curtis, and D. Manocha. 2013. Wave-based sound propagation in large open scenes using an equivalent source formulation. *ACM Transactions on Graphics (TOG)* 32, 2 (2013), 19.

R. Mehra, N. Raghuvanshi, L. Savioja, M. C. Lin, and D. Manocha. 2012. An efficient GPU-based time domain solver for the acoustic wave equation. *Applied Acoustics* 73, 2 (2012), 83 – 94.

A. Meshram, R. Mehra, H. Yang, E. Dunn, J.-M. Frahm, and D. Manochak. 2014. P-hrtf: Efficient personalized hrtf computation for high-fidelity spatial sound. *Mixed and Augmented Reality (ISMAR), 2014 IEEE International Symposium on* (2014).

P. Micikevicius. 2009. 3D Finite Difference Computation on GPUs Using CUDA. In *Proceedings of 2Nd Workshop on General Purpose Processing on Graphics Processing Units (GPGPU-2)*. ACM, New York, NY, USA, 79–84. https://doi.org/10.1145/1513895.1513905

M. Minnaert. 1933. XVI. On musical air-bubbles and the sounds of running water. *The London, Edinburgh, and Dublin Philosophical Magazine and Journal of Science* 16, 104 (1933), 235–248.

R. Mittal, H. Dong, M. Bozkurttas, F. M. Najjar, A. Vargas, and A. Loebbecke. 2008. A versatile sharp interface immersed boundary method for incompressible flows with complex boundaries. *J. Comput. Phys.* 227 (2008).

R. Mittal and G. Iaccarino. 2005. Immersed Boundary Methods. *Annual Review of Fluid Mechanics* 37 (2005).

P. Morse and K. U. Ingard. 1968. *Theoretical Acoustics*. Princeton University Press, Princeton, New Jersey.

W. Moss, H. Yeh, J.-M. Hong, M. C. Lin, and D. Manocha. 2010. Sounding Liquids: Automatic Sound Synthesis from Fluid Simulation. *ACM Trans. Graph.* 29, 3 (2010).

J. F. O'Brien, P. R. Cook, and G. Essl. 2001. Synthesizing Sounds From Physically Based Motion. In *Proceedings of SIGGRAPH 2001*. 529–536.

J. F. O'Brien, C. Shen, and C. M. Gatchalian. 2002. Synthesizing sounds from rigid-body simulations. In *The ACM SIGGRAPH 2002 Symposium on Computer Animation*. ACM Press, 175–181.

C. S. Peskin. 1981. The fluid dynamics of heart valves: experimental, theoretical and computational methods. *Annual Review of Fluid Mechanics* 14 (1981).

N. Raghuvanshi, R. Narain, and M. C. Lin. 2009. Efficient and Accurate Sound Propagation Using Adaptive Rectangular Decomposition. *IEEE Trans. Vis. Comput. Graph.* 15, 5 (2009), 789–801. https://doi.org/10.1109/TVCG.2009.28

N. Raghuvanshi and J. Snyder. 2014. Parametric wave field coding for precomputed sound propagation. *ACM Transactions on Graphics (TOG)* 33, 4 (2014), 38.

J. Saarelma, J. Botts, B. Hamilton, and L. Savioja. 2016. Audibility of dispersion error in room acoustic finite-difference time-domain simulation as a function of simulation distance. *The Journal of the Acoustical Society of America* 139, 4 (2016), 1822–1832.

C. Schissler, R. Mehra, and D. Manocha. 2014. High-order diffraction and diffuse reflections for interactive sound propagation in large environments. *ACM Transactions on Graphics (TOG)* 33, 4 (2014), 39.

C. Schreck, D. Rohmer, D. James, S. Hahmann, and M.-P. Cani. 2016. Real-time sound synthesis for paper material based on geometric analysis. In *Eurographics/ACM SIGGRAPH Symposium on Computer Animation (2016)*.

E. Schweickart, D. L. James, and S. Marschner. 2017. Animating Elastic Rods with Sound. *ACM Transactions on Graphics* 36, 4 (July 2017). https://doi.org/10.1145/3072959.3073680

A. A. Shabana. 2012. *Theory of Vibration: An Introduction*. Springer Science & Business Media.

A. A. Shabana. 2013. *Dynamics of multibody systems*. Cambridge university press.

Side Effects. 2018. Houdini Engine. (2018). http://www.sidefx.com.

J. O. Smith. 1992. Physical modeling using digital waveguides. *Computer music journal* 16, 4 (1992), 74–91.

A. Taflove and S. C. Hagness. 2005. *Computational Electrodynamics: The Finite-Difference Time-Domain Method*. Artech House.

T. Takala and J. Hahn. 1992. Sound rendering. In *Computer Graphics (Proceedings of SIGGRAPH 92)*. 211–220.

J. G. Tolan and J. B. Schneider. 2003. Locally conformal method for acoustic finite-difference time-domain modeling of rigid surfaces. *Journal of the Acoustical Society of America* 114 (2003).

N. Tsingos, T. Funkhouser, A. Ngan, and I. Carlbom. 2001. Modeling acoustics in virtual environments using the uniform theory of diffraction. In *SIGGRAPH '01: Proceedings of the 28th annual conference on Computer graphics and interactive techniques*. ACM, New York, NY, USA, 545–552.

K. van den Doel. 2005. Physically Based Models for Liquid Sounds. *ACM Trans. Appl. Percept.* 2, 4 (Oct. 2005), 534–546. https://doi.org/10.1145/1101530.1101554

K. van den Doel, P. G. Kry, and D. K. Pai. 2001. FoleyAutomatic: Physically-based Sound Effects for Interactive Simulation and Animation. (2001), 537–544. https://doi.org/10.1145/383259.383322

K. van den Doel and D. K. Pai. 1998. The sounds of physical shapes. *Presence: Teleoperators and Virtual Environments* 7, 4 (1998), 382–395.

M. Vorländer. 2008. Auralization. *Aachen: Springer* (2008).

C. J. Webb. 2014. *Parallel computation techniques for virtual acoustics and physical modelling synthesis*. Ph.D. Dissertation.

C. J. Webb and S. Bilbao. 2011. Computing room acoustics with CUDA - 3D FDTD schemes with boundary losses and viscosity. *2011 IEEE International Conference on Acoustics, Speech and Signal Processing (ICASSP)* (2011), 317–320.

H. Yeh, R. Mehra, Z. Ren, L. Antani, D. Manocha, and M. Lin. 2013. Wave-ray Coupling for Interactive Sound Propagation in Large Complex Scenes. *ACM Trans. Graph.* 32, 6, Article 165 (Nov. 2013), 11 pages. https://doi.org/10.1145/2508363.2508420

C. Zheng and D. L. James. 2009. Harmonic Fluids. *ACM Transactions on Graphics (SIGGRAPH 2009)* 28, 3 (Aug. 2009).

C. Zheng and D. L. James. 2010. Rigid-Body Fracture Sound with Precomputed Soundbanks. *ACM Transactions on Graphics (SIGGRAPH 2010)* 29, 3 (July 2010).

C. Zheng and D. L. James. 2011. Toward High-Quality Modal Contact Sound. *ACM Transactions on Graphics (Proceedings of SIGGRAPH 2011)* 30, 4 (Aug. 2011).